

A model for vortical plumes in rotating convection

J. W. Portegies, R. P. Kunnen, G. J. van Heijst, and J. Molenaar

Citation: *Phys. Fluids* **20**, 066602 (2008); doi: 10.1063/1.2936313

View online: <http://dx.doi.org/10.1063/1.2936313>

View Table of Contents: <http://pof.aip.org/resource/1/PHFLE6/v20/i6>

Published by the [American Institute of Physics](#).

Related Articles

Perturbation solution for the viscoelastic 3D flow around a rigid sphere subject to simple shear
Phys. Fluids **23**, 083101 (2011)

The constructal law origin of the logistics S curve
J. Appl. Phys. **110**, 024901 (2011)

The onset of convection in horizontally partitioned porous layers
Phys. Fluids **23**, 064107 (2011)

Flow structure and momentum transport for buoyancy driven mixing flows in long tubes at different tilt angles
Phys. Fluids **23**, 035105 (2011)

Coupling of Kelvin–Helmholtz instability and buoyancy instability in a thermally laminar plasma
Phys. Plasmas **18**, 022110 (2011)

Additional information on Phys. Fluids

Journal Homepage: <http://pof.aip.org/>

Journal Information: http://pof.aip.org/about/about_the_journal

Top downloads: http://pof.aip.org/features/most_downloaded

Information for Authors: <http://pof.aip.org/authors>

ADVERTISEMENT



**Running in Circles Looking
for the Best Science Job?**

Search hundreds of exciting
new jobs each month!

<http://careers.physicstoday.org/jobs>

physicstodayJOBS



A model for vortical plumes in rotating convection

J. W. Portegies,^{1,2} R. P. J. Kunnen,¹ G. J. F. van Heijst,¹ and J. Molenaar^{2,a)}

¹*Department of Physics and J. M. Burgers Centre for Fluid Dynamics, Eindhoven University of Technology, P.O. Box 513, 5600 MB Eindhoven, The Netherlands*

²*Department of Mathematics and Computer Sciences and J. M. Burgers Centre for Fluid Dynamics, Eindhoven University of Technology, P.O. Box 513, 5600 MB Eindhoven, The Netherlands*

(Received 20 March 2008; accepted 29 April 2008; published online 20 June 2008)

In turbulent rotating convection a typical flow structuring in columnar vortices is observed. In the internal structure of these vortices several symmetries are approximately satisfied. A model for these columnar vortices is derived by prescribing these symmetries. The symmetry constraints are applied to the Navier–Stokes equations with rotation in the Boussinesq approximation. It is found that the application of the symmetries results in a set of linearized equations. An investigation of the linearized equations leads to a model for the columnar vortices and a prediction for the heat flux (Nusselt number) that is very appropriate compared to the results from direct numerical simulations of the full governing equations. © 2008 American Institute of Physics. [DOI: 10.1063/1.2936313]

I. INTRODUCTION

Buoyant convection and the Coriolis force caused by the rotation of our Earth are important forces in the flows in the atmosphere and the oceans. A convenient model for such flows, although not fully compatible, is the rotating Rayleigh–Bénard setting: A horizontally infinite layer of fluid is vertically confined by solid walls rotating around a vertical axis, the bottom wall being at a higher temperature than the top wall. Although the lack of a top wall in the geophysical flows makes the model not directly applicable, the general behavior of the model flow shows considerable similarities to real flow in the atmosphere. Furthermore, in the atmosphere the tropopause can be regarded as a “top wall” to a certain extent.

Especially for the large-scale flows in the atmosphere, the effect of the rotation is dominant. The Rossby number, the ratio between inertial and Coriolis forces, is rather small ($O(0.1)$). A well-known theorem valid in rotation-dominated flows was formulated by Proudman¹ and experimentally proven by Taylor;² it is known as the Taylor–Proudman theorem, which states that for inviscid flow in the limit of small Rossby number (the geostrophic flow regime), the vertical component of the velocity gradient is zero, i.e., the flow is vertically uniform. If the influence of buoyancy is also incorporated, it is found that the situation is expanded to the so-called thermal-wind equilibrium,³ which, under the same conditions, essentially states that vertical gradients of the horizontal velocity components are only allowed when horizontal temperature gradients exist. Still, the condition of a uniform vertical velocity component remains. In view of these statements a columnar flow structuring is expected, with active (Ekman) boundary layers connecting the columns to the solid walls. The Ekman layers connect the horizontal

motions in the bulk flow to the no-slip wall, thereby inducing vertical motion that is again independent of the vertical coordinate (as far as the bulk flow outside of the boundary layers is concerned).

Rotating Rayleigh–Bénard convection in the limit of small Rossby number has been the topic of many experimental, numerical, and theoretical studies. Chandrasekhar⁴ studied the onset of convective motion and the flow patterning at onset with linear perturbation theory. Asymptotic expansions in a small parameter are also used in, e.g., Refs. 5 and 6. Experiments with visualizations^{7–11} showed indeed a flow structuring consisting of many columnar vortices. In numerical studies^{12,13} these columnar vortices were also observed.

The prime inspiration for the current investigation stems from another numerical study, the results of which have been partly reported in Ref. 14, where the internal structure of the vortex columns was found to nearly obey certain symmetries. Vertical cross sections of such vortex columns showed that the vertical velocity is nearly symmetric in the midplane, while the vertical vorticity component is antisymmetric in the midplane. For a confined radial extent it seemed also reasonable to consider the vortex column to be independent of the azimuthal orientation. Thus the question arose whether demanding a compliance with these symmetries and conditions would perhaps give solutions to the governing equations, as these solutions would be very helpful for modeling the vortical-convection state and its heat transfer properties. The current work contains the results of this assignment.

Another application area is in deep convection, with related long-lasting vortical chimneys that have been observed in the Greenland Sea.^{15–17} Also, parts of this work might be of interest for problems in spherical-shell convection, relevant for celestial bodies.¹⁸

In Sec. II the governing equations and the problem setting are introduced, along with the dimensionless numbers needed to specify the flow. Some results of a direct numerical simulation (DNS) of these equations are shown in Sec. III. The symmetry considerations and, subsequently, the so-

^{a)}Present address: Biometris (Department for Mathematics and Statistics) and J. M. Burgers Centre for Fluid Dynamics, Wageningen University and Research Centre, P.O. Box 100, 6700 AC Wageningen, The Netherlands.

lution procedure are given in Sec. IV. We present the results of this model with comparison to the DNS results in Sec. V. Section VI contains concluding remarks.

II. PROBLEM SETTING, GOVERNING EQUATIONS, AND DIMENSIONLESS PARAMETERS

Consider a horizontally infinite fluid layer, confined vertically by solid walls a distance H apart. The bottom wall is situated at $z=-H/2$ and is at a temperature $T_0+\Delta T$, while the top wall at $z=H/2$ is at a temperature T_0 . The governing equations for the fluid motion are the Navier–Stokes and heat equations in a rotating reference frame with incompressibility and in the Boussinesq approximation,⁴ where the tildes indicate variables with dimension,

$$\partial_t \tilde{\mathbf{u}} + \tilde{\mathbf{u}} \cdot \tilde{\nabla} \tilde{\mathbf{u}} + 2\Omega \hat{\mathbf{z}} \times \tilde{\mathbf{u}} = -\tilde{\nabla} \tilde{p} + g\alpha \tilde{\theta} \hat{\mathbf{z}} + \nu \tilde{\nabla}^2 \tilde{\mathbf{u}}, \quad (1a)$$

$$\partial_t \tilde{\theta} + \tilde{\mathbf{u}} \cdot \tilde{\nabla} \tilde{\theta} - \frac{\tilde{w} \Delta T}{H} = \kappa \tilde{\nabla}^2 \tilde{\theta}, \quad (1b)$$

$$\tilde{\nabla} \cdot \tilde{\mathbf{u}} = 0, \quad (1c)$$

with $\mathbf{u}=(u,v,w)$ the velocity vector, $\hat{\mathbf{z}}$ the vertical unit vector (the rotation axis and the gravitational acceleration are also aligned vertically), Ω the rotation rate, p the reduced pressure, g the gravitational acceleration, θ the temperature deviation from the conductive profile $T(z)=T_0+(\frac{1}{2}-z/H)\Delta T$, and α , ν , and κ the thermal expansion coefficient, kinematic viscosity, and thermal diffusivity of the fluid, respectively. The equations can be made dimensionless with the length scale H (the separation of the plates), the temperature scale ΔT , and the time scale $\tau=H/U=\sqrt{H/(g\alpha\Delta T)}$ based on the so-called free-fall velocity $U=\sqrt{g\alpha\Delta TH}$. The resulting equations are

$$\partial_t \mathbf{u} + \mathbf{u} \cdot \nabla \mathbf{u} + \sqrt{\frac{\sigma \text{Ta}}{\text{Ra}}} \hat{\mathbf{z}} \times \mathbf{u} = -\nabla p + \theta \hat{\mathbf{z}} + \sqrt{\frac{\sigma}{\text{Ra}}} \nabla^2 \mathbf{u}, \quad (2a)$$

$$\partial_t \theta + \mathbf{u} \cdot \nabla \theta - w = \frac{1}{\sqrt{\sigma \text{Ra}}} \nabla^2 \theta, \quad (2b)$$

$$\nabla \cdot \mathbf{u} = 0, \quad (2c)$$

where all symbols now denote dimensionless variables. The following dimensionless parameters have been introduced: The Rayleigh number $\text{Ra} \equiv g\alpha\Delta TH^3/(\nu\kappa)$, the Taylor number $\text{Ta} \equiv (2\Omega H^2/\nu)^2$, and the Prandtl number $\sigma \equiv \nu/\kappa$. Another important parameter in the following denotes the importance of the buoyancy force relative to the Coriolis force: The Rossby number $\text{Ro} \equiv U/(2\Omega H) = \sqrt{\text{Ra}/(\sigma \text{Ta})}$.

The boundary conditions on the plates are prescribed as follows:

$$\mathbf{u} = \mathbf{0}, \quad z = \pm \frac{1}{2}, \quad \theta = 0, \quad z = \pm \frac{1}{2}. \quad (3)$$

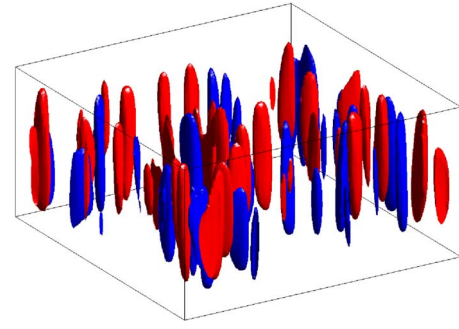


FIG. 1. (Color online) Isosurfaces of $w = \pm 0.07$. The red (light gray) surfaces indicate upward motion; blue (dark gray) is for downward motion.

III. DNS OF THE EQUATIONS

The Equations (2a)–(2c) can be used for DNS. Such a study was undertaken before; the results have been partly reported in Ref. 14. The equations were solved on an $L_x \times L_y \times L_z = 2 \times 2 \times 1$ domain with a fourth-order accurate finite-difference scheme. Boundary conditions were as in Eq. (3). The horizontal directions were periodic to emulate a horizontally unbounded layer of fluid. For further details on the numerical procedure, we refer to Ref. 14.

Here we provide a typical image from a simulation using $\text{Ra} = 2.5 \times 10^6$, $\sigma = 1$, and $\text{Ta} = 10^8$. In this case $\text{Ro} = 0.158$, thus a strong rotational constraint is expected. An isosurface plot of the vertical velocity component in Fig. 1 shows the columnar flow structuring typical of rotation-dominated turbulent convection. The red (light gray) surfaces are for $w = +0.07$, so for columns with upward motion, while the blue (dark gray) surfaces at $w = -0.07$ are for columns with downward motion. The number of columns with upward and downward motions is roughly equal. Also the sizes are similar. This is expected given the inherent symmetries of the Boussinesq equations. The columnar structuring due to rotation was found in all simulations for which $\text{Ro} \lesssim 0.5$. This can be taken as the border of the range of validity for the current work.

From these simulations it was found that the vortex columns show approximate symmetry in the midplane. As a first-order approximation the vertical vorticity component ω_z inside the column is antisymmetric in $z=0$, while u_z is roughly symmetric in $z=0$. The temperature, after subtraction of the conductive profile $\theta = T - (\frac{1}{2} - z)$, shows more deviations from symmetry, but we still assume symmetry in $z=0$ as a first approximation. [The ensemble-averaged profiles of 40 columns with upward motion are shown later, in Fig. 6(a). These symmetries were found to be also valid for the “downward” columns.] The observation of the approximate symmetries was the principal motivation for the current work.

IV. A HEURISTIC MODEL

It is profitable to proceed with cylindrical coordinates (r, ϕ, z) and the associated velocity vector (u_r, u_ϕ, u_z) . Our objective is thus to search for (i) axisymmetric, (ii) steady (viz., time independent), and (iii) vertically symmetric solutions according to

$$u_r(r, z) = -u_r(r, -z), \quad (4a)$$

$$u_\phi(r, z) = -u_\phi(r, -z), \quad (4b)$$

$$u_z(r, z) = u_z(r, -z), \quad (4c)$$

$$\theta(r, z) = \theta(r, -z). \quad (4d)$$

Under the assumption of axial symmetry all ϕ derivatives are zero, and the steadiness of the solution implies vanishing of the time derivatives. In view of the prescribed symmetries, Eqs. (2a)–(2c) split up in even and odd parts that vanish separately. This results in

$$-\sqrt{\frac{\sigma\text{Ta}}{\text{Ra}}}u_\phi = -\partial_r p + \sqrt{\frac{\sigma}{\text{Ra}}}\left(\nabla^2 - \frac{1}{r^2}\right)u_r, \quad (5a)$$

$$\sqrt{\frac{\sigma\text{Ta}}{\text{Ra}}}u_r = \sqrt{\frac{\sigma}{\text{Ra}}}\left(\nabla^2 - \frac{1}{r^2}\right)u_\phi, \quad (5b)$$

$$0 = -\partial_z p + \theta + \sqrt{\frac{\sigma}{\text{Ra}}}\nabla^2 u_z, \quad (5c)$$

$$-u_z = \frac{1}{\sqrt{\sigma\text{Ra}}}\nabla^2 \theta, \quad (5d)$$

$$\partial_r u_r + \frac{u_r}{r} + \partial_z u_z = 0, \quad (5e)$$

and the conditions that all nonlinear parts be zero. Thus the symmetries lead to the linearized versions of the governing equations. Note that a solution of Eqs. (5a)–(5e) probably does not satisfy the full equations including the nonlinear terms. Still, as a heuristic model we continue with the linearized equations. The linear set of equations is often used in studies concerning the onset of convection, e.g., Refs. 4, 19, and 20. In this case, however, an alternative solution procedure is applied in view of the axial symmetry, leading to a new solution.

Because of Eq. (5e) it is possible to introduce a streamfunction $\psi(r, z)$ according to

$$u_r = -\frac{1}{r}\partial_z \psi, \quad u_z = \frac{1}{r}\partial_r \psi. \quad (6)$$

In view of Eqs. (4a) and (4c) ψ is even in z . The boundary conditions for ψ are $\partial_z \psi = \partial_r \psi = 0$ at $z = \pm \frac{1}{2}$.

We can now eliminate p by cross differentiation of Eqs. (5a) and (5c). Three equations remain,

$$\sqrt{\frac{\sigma\text{Ta}}{\text{Ra}}}\partial_z u_\phi = \partial_r \theta + \frac{1}{r}\sqrt{\frac{\sigma}{\text{Ra}}}\left(\nabla^2 - \frac{2}{r}\partial_r\right)^2 \psi, \quad (7a)$$

$$-\sqrt{\frac{\sigma\text{Ta}}{\text{Ra}}}\partial_z \psi = r\sqrt{\frac{\sigma}{\text{Ra}}}\left(\nabla^2 - \frac{1}{r^2}\right)u_\phi, \quad (7b)$$

$$-\partial_r \psi = \frac{r}{\sqrt{\sigma\text{Ra}}}\nabla^2 \theta. \quad (7c)$$

Next, we try to separate variables and write the solution as the product of a function depending on z and a function depending on r . For the latter, radial part we take either $J_0(kr)$ (even symmetry) or $J_1(kr)$ (odd symmetry). Here J_0 and J_1 are Bessel functions of orders of 0 and 1, respectively, and k is a constant to be determined later on. In particular, we use the following ansatz:

$$\psi = krJ_1(kr)\Psi(z), \quad (8a)$$

$$u_\phi = J_1(kr)\Phi(z), \quad (8b)$$

$$\theta = J_0(kr)\Theta(z). \quad (8c)$$

The boundary conditions translate to

$$\Phi = \Theta = \Psi = \Psi' = 0, \quad z = \pm \frac{1}{2}. \quad (9)$$

We insert these trial functions into the set (7). By use of the well-known properties

$$\partial_x[x^m J_m(x)] = x^m J_{m-1}(x)$$

and

$$J_{-m}(x) = (-1)^m J_m(x),$$

valid for integer values of m , we find that the dependence on the radial coordinate r drops out. What remains are three linear ordinary differential equations in terms of the vertical coordinate z ,

$$\sqrt{\frac{\sigma\text{Ta}}{\text{Ra}}}\Phi' = -k\Theta + k\sqrt{\frac{\sigma}{\text{Ra}}}(\partial_{zz} - k^2)^2 \Psi, \quad (10a)$$

$$-k\sqrt{\text{Ta}}\Psi' = (\partial_{zz} - k^2)\Phi, \quad (10b)$$

$$-k^2\sqrt{\sigma\text{Ra}}\Psi = (\partial_{zz} - k^2)\Theta. \quad (10c)$$

By differentiating Eq. (10b) once, applying the operator $(\partial_{zz} - k^2)$ to Eq. (10a), and substituting, we arrive at a single sixth-order differential equation concerning just Ψ ,

$$(\partial_{zz} - k^2)^3 \Psi + \text{Ta}\Psi'' + k^2\text{Ra}\Psi = 0. \quad (11)$$

Equation (11) can be solved by substituting $\Psi = \exp(\lambda z)$ and finding the roots of the characteristic equation,

$$\lambda^6 - 3k^2\lambda^4 + (3k^4 + \text{Ta})\lambda^2 + k^2\text{Ra} - k^6 = 0. \tag{12}$$

The roots of the cubic equation in $x \equiv \lambda^2$ are

$$x_1 = k^2 - \frac{2^{1/3}\text{Ta}}{\zeta} + \frac{\zeta}{3(2^{1/3})}, \tag{13a}$$

$$x_2 = k^2 + \frac{(1 + i\sqrt{3})\text{Ta}}{2^{2/3}\zeta} - \frac{(1 - i\sqrt{3})\zeta}{6(2^{1/3})}, \tag{13b}$$

$$x_3 = x_2^*, \tag{13c}$$

where * denotes complex conjugation and the symbol ζ is used to represent the real, positive constant,

$$\zeta \equiv [\sqrt{108\text{Ta}^3 + 27^2k^4(\text{Ra} + \text{Ta})^2 - 27k^2(\text{Ra} + \text{Ta})}]^{1/3}.$$

Since only the real parts of these solutions are relevant for the current problem the roots are written in a slightly different way. We introduce the constants f , g , and h as

$$f \equiv \frac{1}{2}\sqrt{2\sqrt{|x_2|} + \Re(x_2)},$$

$$g \equiv \frac{1}{2}\sqrt{2\sqrt{|x_2|} - \Re(x_2)},$$

$$h \equiv \sqrt{-x_1}.$$

The minus sign in the definition of h is put there since positive values of x_1 give unphysical solutions, so that relevant values of h are now real. Concerning f and g , it holds that

$$x_2 = [\pm(f + ig)]^2,$$

$$x_3 = [\pm(f - ig)]^2.$$

The general solution reads as

$$\begin{aligned} \Psi = & a_1 \cos(hz) + a_2 \sinh(fz)\sin(gz) + a_3 \cosh(fz)\cos(gz) \\ & + a_4 \sinh(fz)\cos(gz) + a_5 \cosh(fz)\sin(gz) \\ & + a_6 \sin(hz), \end{aligned} \tag{14}$$

where the coefficients $a_{1,2,3}$ are for the even parts, while $a_{4,5,6}$ are for the odd parts. The odd parts can be taken out since Ψ must be even, which implies that $a_4 = a_5 = a_6 = 0$. From Eq. (10b) a similar notation is now obtained for Φ , with the even parts already left out as Φ is odd,

$$\begin{aligned} \Phi = & b_1 \sinh(kz) + b_2 \sin(hz) + b_3 \sinh(fz)\cos(gz) \\ & + b_4 \cosh(fz)\sin(gz). \end{aligned} \tag{15}$$

Coefficients $b_{2,3,4}$ are found in terms of $a_{1,2,3}$ from Eq. (10b),

$$b_2 = -a_1\sqrt{\text{Ta}}\frac{hk}{h^2 + k^2},$$

$$b_3 = k\sqrt{\text{Ta}}\frac{(a_2g - a_3f)(f^2 + g^2) + (a_2g + a_3f)k^2}{(f^2 - g^2 - k^2)^2 + 4f^2g^2},$$

$$b_4 = -k\sqrt{\text{Ta}}\frac{(a_2f + a_3g)(f^2 + g^2) - (a_2f - a_3g)k^2}{(f^2 - g^2 - k^2)^2 + 4f^2g^2}.$$

The coefficient b_1 is not determined by $a_{1,2,3}$ and needs to be solved along with these coefficients. Similarly, Θ is written as

$$\begin{aligned} \Theta = & c_1 \cos(hz) + c_2 \sinh(fz)\sin(gz) + c_3 \cosh(fz)\cos(gz) \\ & + c_4 \cosh(kz). \end{aligned} \tag{16}$$

With Eqs. (10a) and (10c) $c_1 - c_4$ can be fully expressed in terms of the previous unknowns,

$$c_1 = k^2\frac{\sqrt{\sigma\text{Ra}}}{h^2 + k^2}a_1,$$

$$c_2 = -k^2\sqrt{\sigma\text{Ra}}\frac{2a_3fg + a_2(f^2 - g^2 - k^2)}{(f^2 - g^2 - k^2)^2 + 4f^2g^2},$$

$$c_3 = -k^2\sqrt{\sigma\text{Ra}}\frac{a_3(f^2 - g^2 - k^2) - 2a_2fg}{(f^2 - g^2 - k^2)^2 + 4f^2g^2},$$

$$c_4 = -\sqrt{\frac{\sigma\text{Ta}}{\text{Ra}}}b_1.$$

Now the boundary conditions are applied. Note that, because of symmetry, only the boundary conditions at $z = \frac{1}{2}$ are evaluated; the conditions at $z = -\frac{1}{2}$ are then automatically satisfied. We introduce a matrix M such that the boundary conditions are

$$M \cdot \begin{pmatrix} a_1 \\ a_2 \\ a_3 \\ b_1 \end{pmatrix} = 0. \tag{17}$$

M has the rather unwieldy shape

$$M = \begin{pmatrix} \cos\left(\frac{h}{2}\right) & \sinh\left(\frac{f}{2}\right)\sin\left(\frac{g}{2}\right) & \cosh\left(\frac{f}{2}\right)\cos\left(\frac{g}{2}\right) & 0 \\ -h\sin\left(\frac{h}{2}\right) & f\cosh\left(\frac{f}{2}\right)\sin\left(\frac{g}{2}\right) + g\sinh\left(\frac{f}{2}\right)\cos\left(\frac{g}{2}\right) & f\sinh\left(\frac{f}{2}\right)\cos\left(\frac{g}{2}\right) - g\cosh\left(\frac{f}{2}\right)\sin\left(\frac{g}{2}\right) & 0 \\ k^2\sqrt{\sigma\text{Ra}}\frac{\cos\left(\frac{h}{2}\right)}{h^2 + k^2} & k^2\sqrt{\sigma\text{Ra}}\frac{2fg\cosh\left(\frac{f}{2}\right)\cos\left(\frac{g}{2}\right) - (f^2 - g^2 - k^2)\sinh\left(\frac{f}{2}\right)\sin\left(\frac{g}{2}\right)}{(f^2 - g^2 - k^2)^2 + 4f^2g^2} & -k^2\sqrt{\sigma\text{Ra}}\frac{2fg\sinh\left(\frac{f}{2}\right)\sin\left(\frac{g}{2}\right) + (f^2 - g^2 - k^2)\cosh\left(\frac{f}{2}\right)\cos\left(\frac{g}{2}\right)}{(f^2 - g^2 - k^2)^2 + 4f^2g^2} & -\sqrt{\frac{\sigma\text{Ta}}{\text{Ra}}}\cosh\left(\frac{k}{2}\right) \\ -k\sqrt{\text{Ta}}\frac{h\sin\left(\frac{h}{2}\right)}{h^2 + k^2} & k\sqrt{\text{Ta}}\frac{g(f^2 + g^2 + k^2)\sinh\left(\frac{f}{2}\right)\cos\left(\frac{g}{2}\right) - f(f^2 + g^2 - k^2)\cosh\left(\frac{f}{2}\right)\sin\left(\frac{g}{2}\right)}{(f^2 - g^2 - k^2)^2 + 4f^2g^2} & -k\sqrt{\text{Ta}}\frac{f(f^2 + g^2 - k^2)\sinh\left(\frac{f}{2}\right)\cos\left(\frac{g}{2}\right) + g(f^2 + g^2 + k^2)\cosh\left(\frac{f}{2}\right)\sin\left(\frac{g}{2}\right)}{(f^2 - g^2 - k^2)^2 + 4f^2g^2} & \sinh\left(\frac{k}{2}\right) \end{pmatrix}. \tag{18}$$

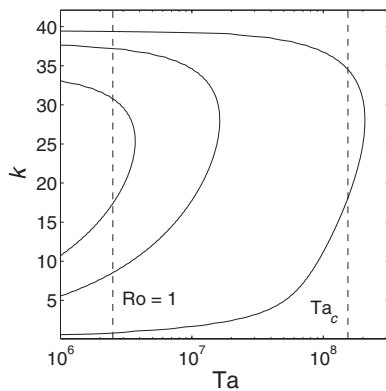


FIG. 2. Values of k as a function of Ta for $Ra=2.5 \times 10^6$, $\sigma=1$. Also included (dashed lines) are the Chandrasekhar stability value $Ta_c=1.54 \times 10^8$ and the position where $Ro=1$.

With given Ra , Ta , and σ , the determinant of M vanishes for values of k that form nontrivial solutions. These roots can be found with iterative numerical methods. Finally, to obtain a solution we must determine the constants $a_{1,2,3}$ and b_1 . Three of these can be expressed in terms of the fourth; here we write $a_{2,3}$ and b_1 in terms of a_1 , where M_{ij} denote the individual matrix elements of M ,

$$a_2 = \frac{M_{13}M_{21} - M_{11}M_{23}}{M_{12}M_{23} - M_{13}M_{22}} a_1,$$

$$a_3 = \frac{M_{12}M_{21} - M_{11}M_{22}}{M_{13}M_{22} - M_{12}M_{23}} a_1,$$

$$b_1 = \frac{a_1}{M_{12}M_{23}M_{34} - M_{13}M_{22}M_{34} - M_{12}M_{23}M_{31} - M_{13}M_{21}M_{32} + M_{11}M_{23}M_{32} + M_{12}M_{21}M_{33} - M_{11}M_{22}M_{33}}.$$

The last unknown constant a_1 is a free parameter. An upper bound for a_1 can be given on physical grounds by demanding that the temperature $\theta + \frac{1}{2}z$ remains between 0 and 1 for all z . This will be used later on to give an upper bound for the heat transfer through the vortical plume.

V. RESULTS OF THE MODEL

In this section we first show the general shape of the model solution. A comparison to the DNS is carried out, with variation of the governing parameters. Finally, an upper bound for the heat flux through an array of vortices is derived.

The first case we consider is for fixed values $Ra=2.5 \times 10^6$, $\sigma=1$. This is equal to the parameters used in Ref. 14. Figure 2 shows the values of k as a function of Ta . There are two limits to the parameters that are applied here. The first gives an upper limit for Ta as a function of Ra ; it is the Chandrasekhar stability criterion for onset of convection $Ra_c \approx 8.7Ta_c^{2/3}$.⁴ For given Ta , Ra must be larger than Ra_c for convection to set in. It is found that the highest allowable Ta value that allows a solution in the model ($Ta=2.08 \times 10^8$ at $k=28.1$) matches rather well with the Chandrasekhar limit

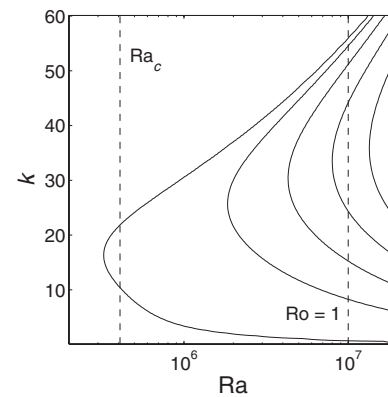


FIG. 3. Values of k as a function of Ra for $Ta=1 \times 10^8$, $\sigma=1$. Also included (dashed lines) are the Chandrasekhar stability value $Ra_c=1.87 \times 10^6$ and the position where $Ro=1$.

value $Ta_c=1.54 \times 10^8$. We choose a lower limit of Ta by demanding that the flow is rotation dominated, i.e., $Ro \leq 1$ and thus $Ra \leq \sigma Ta$.

Another observation considers the growing number of possible solutions as Ta decreases. Then, two branches are formed: One at $k \approx 39$, the “narrow vortex,” and another with a stronger dependence on Ta , the “wide vortex.” Of the two, the narrow-vortex solution is of interest here because it is most comparable to the DNS results. Indeed, for the wide vortex its radius $r_0 \sim 1/k$ grows very large, even at moderate Ta . This is not what is captured in the DNS, where far narrower plumes are found at all relevant Ta values. Furthermore, velocity values for the wide vortex are very small, while the motions in the DNS vortices are considerably more vigorous. Therefore, the focus will be on the narrow vortex, while the wide vortex is also a physically allowable solution. For $Ta \lesssim 1.5 \times 10^7$ another pair of k values is found. These correspond to solutions that are less relevant in this context since the resulting structures are composed of more than a single cell in the vertical direction, i.e., the vertical velocity is not of one sign throughout the vertical extent. The growing number of allowed k values is possibly an indication of the growing instability of the vortex solutions, as more and more three-dimensional structuring is allowed at lower dimensionless rotation rates Ta .

Variation of Ra is covered in Fig. 3. For this plot fixed values $Ta=1 \times 10^8$ and $\sigma=1$ are chosen. Again the applicability of the current model is bounded by the Chandrasekhar limit Ra_c and the condition of rotation-dominated flow $Ro \leq 1$, both indicated with dashed lines. A similar picture arises, with two branches of allowable k values, deviating as Ra increases. At higher $Ra \gtrsim 8 \times 10^6$ additional solutions are found; these are again solutions with more complicated vertical structuring and thus are not relevant here.

The allowed k values are independent of σ . The σ dependence is present only in a single row of M , and hence can be factored out of $\det(M)=0$.

As an example case for the spatial structure of the vortex solution we choose $Ta=10^8$, with $Ra=2.5 \times 10^6$ and $\sigma=1$ as before. The relevant k value comes from the upper branch of solutions in Fig. 2; for the current parameters $k=36.8$. With the k value the model solution is fully determined but for the

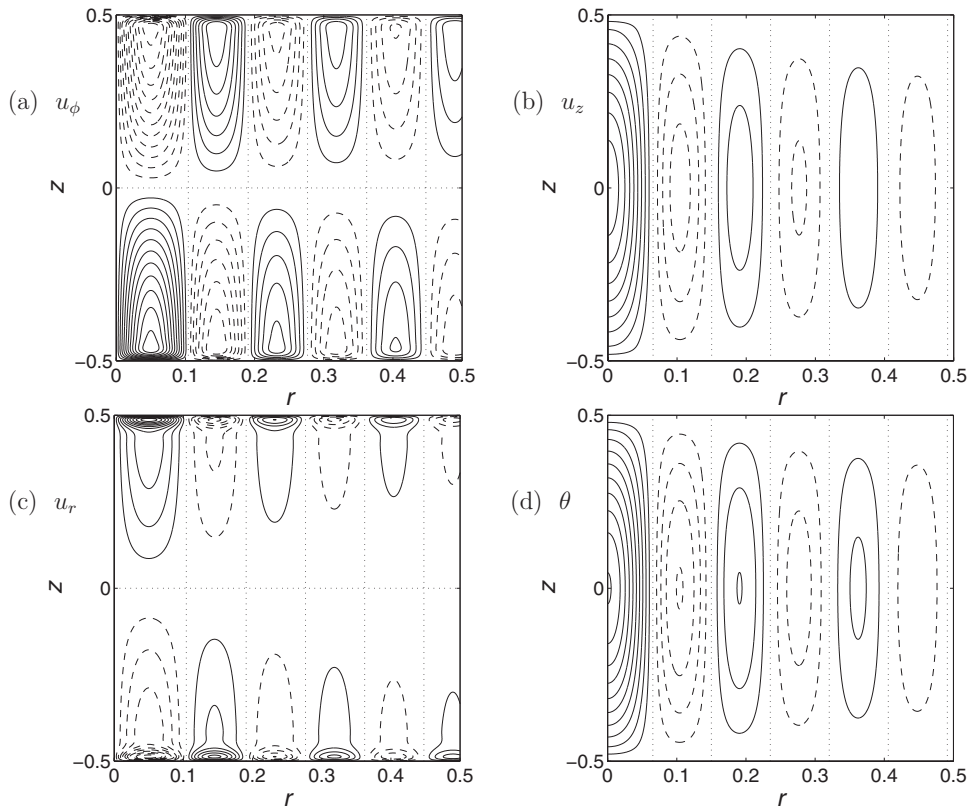


FIG. 4. Radial-vertical cross-sectional plots of the vortex solution at $Ra=2.5 \times 10^6$, $Ta=10^8$, and $\sigma=1$. The solid contours indicate positive values, while dashed contours are for negative values. The dotted lines are the zero contours. (a) Azimuthal velocity u_ϕ , with contour increment of 0.005. (b) Vertical velocity u_z , contour increment of 0.02. (c) Radial velocity u_r , contour increment of 0.002. (d) Temperature deviation θ from the conductive profile, with contour increment of 0.02.

constant a_1 . We wish to restrict the results to just the “warm” vortices that are responsible for upward transport of fluid and heat and are of higher-than-average temperature. The corresponding “cold” vortex solution follows straightforwardly from symmetry. For the warm vortex, by demanding that temperature T remains below the boundary value $T=1$ for all z , we can derive an upper bound for a_1 : For the current parameter set we arrive at $a_1=1.28 \times 10^{-4}$.

To give a visual impression of the solution, contour plots of u_r , u_ϕ , u_z , and θ are presented as a function of r and z in Fig. 4. Another important result for the vortex solution is the vertical component of vorticity ω_z , easily calculated from u_ϕ as $\omega_z=(1/r)\partial_r(ru_\phi)$ given the symmetry. It is presented in Fig. 5. The solutions have vertically dominant sine-or cosine-

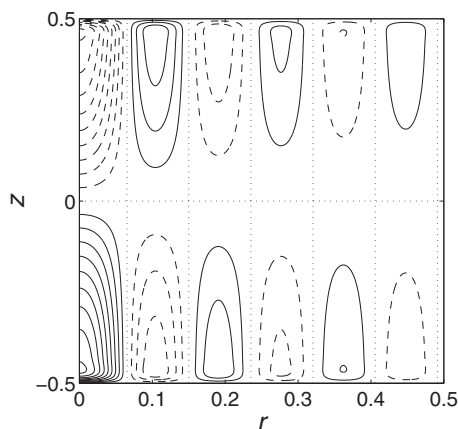


FIG. 5. Plot of vertical vorticity ω_z of the vortex solution. $Ra=2.5 \times 10^6$, $Ta=10^8$, and $\sigma=1$. Lines as in Fig. 4, but now with contour increment of 0.4.

like behavior in the bulk with boundary layers to connect to the walls. In the radial direction the Bessel function profiles are readily recognized.

We can compare the model solution at $Ra=2.5 \times 10^6$, $Ta=1 \times 10^8$, and $\sigma=1$, as introduced in Figs. 4 and 5, to actual vortices found in the DNS. An ensemble average of 40 warm vortices, found in the DNS, has been carried out. Vertical profiles taken at the horizontal position of the center of the vortices of vertical velocity u_z , vertical vorticity ω_z , and temperature T are shown in Fig. 6(a). In Fig. 6(b) the corresponding profiles from the model are given. Similarly, in Fig. 7(a) a horizontal profile of the average DNS vortex at height $z \approx -0.25$ is presented, with the corresponding model profiles displayed in Fig. 7(b). The horizontal profiles also include azimuthal velocity u_ϕ . Note that the model vortex is an “upper limit” in terms of the constant a_1 , so that the DNS vortex will generally have lower temperature, velocity, and vorticity.

The qualitative comparison is quite favorable, but there are several differences to be found. The vertical symmetry is not exactly followed in DNS. However, as a first-order approximation it is definitely applicable. Also, the radius of the vortex in DNS is somewhat wider than in the model. The first zero crossings in the horizontal profiles of u_z or ω_z are found at $r \approx 0.066$ in the model and at $r \approx 0.090$ in the DNS vortex. The vertical velocity is about a factor of 2 larger in the model than in DNS, while the maximal azimuthal velocity is almost equal for the two cases. The vertical-vorticity profiles match well, apart from an asymmetric offset in the vertical profile in the DNS vortex. An oppositely signed shield is found for larger $r > 0.090$ in the DNS vortex. At the outer edge of this shield the velocities and vorticity tend to

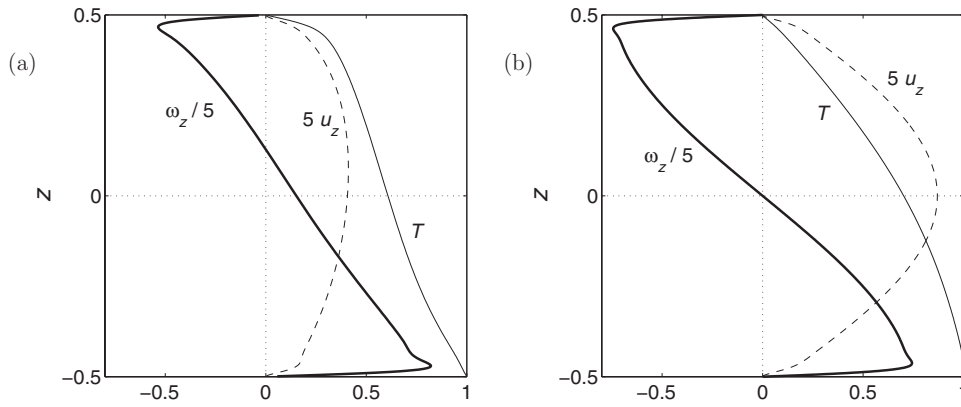


FIG. 6. (a) Vertical profiles of vertical velocity u_z (dashed line; multiplied by 5), vertical vorticity ω_z (thick solid line; divided by 5), and temperature T (thin solid line), from the ensemble-averaged DNS vortex column. (b) Corresponding profiles from the current vortex model.

zero. The shield may be represented in the model by extending the radial extent to $r_0 \equiv j_{0,2}/k$ (the notation $j_{0,2}$ is used to indicate the second zero of J_0 : $j_{0,2} \approx 5.52$), as is done in Fig. 7(b) with $r_0 \approx 0.15$. The sharp edge is unphysical, but again it should be regarded a first-order approximation to the DNS vortex.

The heat flux of convective systems is usually expressed by the Nusselt number Nu , the total heat flux normalized by the conductive heat flux that is present in a quiescent fluid. In the current units Nu is defined as

$$Nu \equiv \left\langle \frac{\partial T}{\partial z} \right\rangle + \sqrt{\sigma Ra} \langle u_z T \rangle,$$

where the angular brackets indicate averaging over a horizontal cross section of the fluid layer. The intersection is taken at $z=0$, the central plane. What remains of Nu is then

$$Nu = 1 + \sqrt{\sigma Ra} \langle u_z \theta \rangle. \tag{19}$$

To calculate Nu for the model, the following assumptions are made.

- (1) As before, the value of a_1 is taken the maximal value that still complies with the condition $T \leq 1$. This gives an upper bound on a_1 , and thus also on Nu .
- (2) There are equally many warm as cold vortices. This has been verified from the DNS.
- (3) Each vortex is radially terminated at r_0 . This is done to create a shield. We remark here that taking higher zeroes

of J_0 would lead to radial profiles incompatible with the DNS results, as there is just one shield to be found.

- (4) The entire cross-sectional area is filled with a closest-packed hexagonal grid of circular vortices. Again, this situation provides an upper bound as real snapshots from DNS show a sparser vortex distribution. By the model symmetry, contributions from warm and cold vortices are identical. Hence, this assumption allows the averaging to be constrained to just a single model vortex, with the area of consideration being one hexagon of inner radius r_0 and area $2\sqrt{3}r_0^2$. Another implication of this assumption that will be discussed later is that the vortex number density N scales as $N \sim r_0^{-2}$.

We arrive at

$$Nu = 1 + \frac{\sqrt{\sigma Ra}}{2\sqrt{3}r_0^2} \int_0^{r_0} \Theta(0) J_0(kr') \cdot \Psi(0) \frac{\partial_r [kr' J_1(kr')]}{r'} \times 2\pi r' dr',$$

which finally reduces to

$$Nu = 1 + \frac{\pi\sqrt{\sigma Ra}}{2\sqrt{3}} \Theta(0)\Psi(0)k^2 J_1(j_{0,2})^2. \tag{20}$$

A calculation of the upper bound on Nu for various Ta at $Ra = 2.5 \times 10^6$, $\sigma = 1$ has been carried out. The results are indicated with the thick solid line in Fig. 8. Also included are

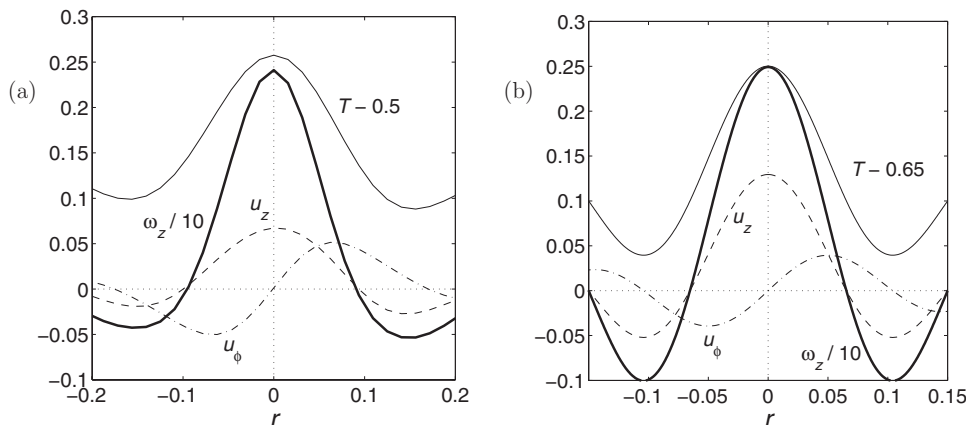


FIG. 7. (a) Horizontal profiles of vertical velocity u_z (dashed line), temperature T (thin solid line; shifted downward by 0.5), vertical vorticity ω_z (thick solid line; divided by 10), and azimuthal velocity u_ϕ (dash-dotted line; it is the velocity component in the horizontal plane perpendicular to the cross-sectional line) taken at $z = -0.25$ through the ensemble-averaged DNS vortex column. (b) Corresponding profiles from the current vortex model; the temperature curve (thin solid line) is shifted downward by 0.65 instead.

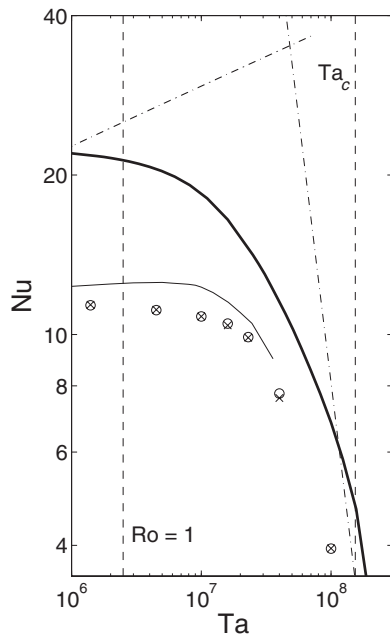


FIG. 8. Dependence of Nu on Ta for $Ra=2.5 \times 10^6$, $\sigma=1$. The thick solid line indicates the current result. The crosses and circles are taken from Ref. 14 (values of Nu calculated from the average temperature derivative at the walls). The thin solid line is the experimental result of Ref. 21 in water ($\sigma \approx 7$). The dash-dotted line is an upper bound for $\sigma \rightarrow \infty$ obtained with a variational method in Ref. 22. Again the position of the critical Taylor number Ta_c and the position at which $Ro=1$ are indicated with dashed lines.

results from the DNS (Ref. 14) (crosses and circles), results from an experiment in water at $\sigma \approx 7$ (Ref. 21) (thin solid line), and an upper bound at $\sigma \rightarrow \infty$ obtained with a variational method (Ref. 22) (dash-dotted line). It is found that the current model overestimates the heat flux by about a factor of 2. Given the unknown constant a_1 and the assumptions of the radial cutoff and tightly packed coverage of the fluid layer with vortices this is indeed a satisfying result. It is comparable to the result of Ref. 22 except for the small growth of Nu at moderate Ta. At the larger Ta values the steep decrease of Nu is well represented.

We now compare the effects of variation of Ta between the current theory and the DNS. As can be seen in Fig. 2, the relevant value of k (the upper branch of solutions) remains almost constant when Ta changes, so that vortices are expected to be of similar size for all Ta considered. A comparison of DNS snapshots at $Ta=1 \times 10^7$ and 1×10^8 revealed that indeed in both cases on average roughly the same number of vortices can be identified (by visual inspection). However, at $Ta=1 \times 10^7$ the rotational constraint is less stringent and more vertical variation is found in the velocity, temperature, and vorticity profiles. Also, at this lower rotation rate the velocities inside the vortices are higher, as is the temperature contrast with the surroundings, such that the heat transfer (Nu) is considerably higher.

Variation of Ra is also straightforward in the model, see Fig. 9. The solid line indicates the model result at $Ta=1 \times 10^8$, $\sigma=1$, while the circles are the corresponding values from DNS. The rapid drop in the model curve near Ra_c is an indication of the model reaching the Rayleigh number where no vortex solution is allowed, see also Fig. 3 where for

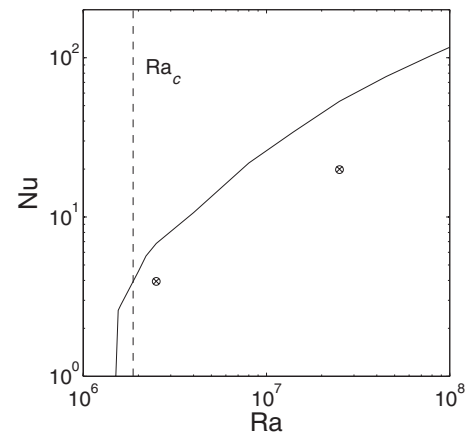


FIG. 9. Dependence of Nu on Ra at constant $Ta=1 \times 10^8$ and $\sigma=1$. The solid line indicates the model result. The circles and crosses are DNS results from Ref. 14. The position of the critical Rayleigh number Ra_c is indicated with the dashed line.

$Ra \leq 1.5 \times 10^6$ no suitable k value can be found. At higher Ra it is found that the upper bound on Nu obtained from the model has a somewhat larger separation from the DNS result, but is still very much applicable. Extension to even higher Ra is unfeasible, as then the constraint $Ro \leq 1$ is crossed.

An additional effect of the variation of Ra can be appreciated from Fig. 3. With increasing Ra the relevant k value also increases. This means that the typical vortex size must decrease. In other words, the vortex density increases with increasing Ra. If we define a typical vortex density as $N=r_0^{-2}=(j_{0,2}/k)^2$ and compare these for $Ra=2.5 \times 10^6$ and 2.5×10^7 , then in the model the higher-Ra case has 3.67 times as many vortices as the lower-Ra case. Visual inspection of DNS snapshots indeed showed that the vortices are smaller at higher Ra, but the factor of 3.67 was not recovered. Instead, the higher-Ra case had on average slightly more than two times as many vortices as at the lower Ra. This may explain the larger model overprediction of Nu at higher Ra compared to the DNS result.

Another approach is to investigate variation of Ra with an additional constraint that the ratio of buoyancy and rotation, i.e., the Rossby number Ro , remains the same. At a constant Prandtl number, Ra and Ta are varied such that $Ro \sim \sqrt{Ra/Ta}$ remains constant. This approach was followed before in literature, e.g., Refs. 12 and 23. In Fig. 10 the dependence of Nu on Ra (and thus, implicitly, Ta) is shown, while keeping Ro constant. This is plotted for three separate values of Ro . Also included are our DNS results at $Ro=0.75$ (circles and crosses). The three curves at different Ro are roughly parallel; a power-law fit of the slopes results in $Nu \sim Ra^{0.57}$ at $Ro=0.1$, $Nu \sim Ra^{0.48}$ at $Ro=0.2$, and $Nu \sim Ra^{0.47}$ at $Ro=0.75$. In the $Ro=0.1$ curve the sudden decrease to $Nu=1$ at $Ra \approx 3.5 \times 10^6$ occurs because no solution of the model is found anymore, cf. Figs. 3 and 9. When comparing these slopes to results from the DNS of Ref. 12 or the experiments of Ref. 23 (in both studies $Nu \sim Ra^{0.27}$ is found) it is found that the model progressively overestimates the heat flux at larger Ra for constants Ro and σ ; or the bound becomes less and less stringent.

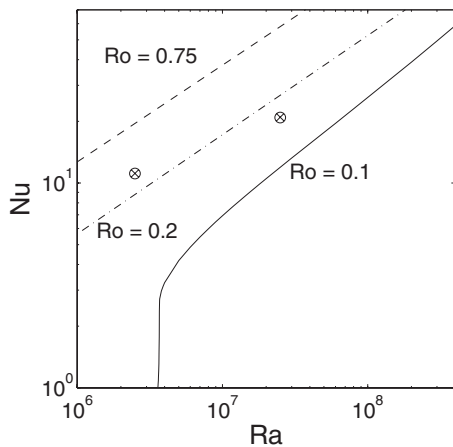


FIG. 10. Dependence of Nu on Ra at constant $\sigma=1$ and for constant $Ro=0.1$ (solid line), $Ro=0.2$ (dash-dotted line), and $Ro=0.75$ (dashed line). The circles and crosses indicate DNS results of Ref. 14 at $Ro=0.75$, $\sigma=1$.

A final consideration is the variation of σ and its effect on Nu . This is depicted in Fig. 11, at constant $Ra=2.5 \times 10^6$ and constant $Ro=0.5$. On the lower- σ side again a critical value for convection is found from the model (where Nu becomes larger than 1), close to the Chandrasekhar stability limit (in this case a critical Prandtl number $\sigma_c=0.0649$). The higher- σ side has a power-law behavior as $Nu \sim \sigma^{-0.38}$. The inset shows $Nu(\sigma)$, now at constant $Ra=2.5 \times 10^6$ and constant $Ta=1 \times 10^8$. A fit is $Nu \sim \sigma^{-0.42}$. In both cases Nu is a decreasing function of σ (except for the region around the stability limit). Yet, in other studies a different correlation is found. In the experiments of Rossby²¹ rotating heat transfer at two different σ is considered: $\sigma=0.025$ and 6.8 . Nu was found to be larger at the higher $\sigma=6.8$. This trend was also reported from simulations of nonrotating convection.^{24,25} The model does not reproduce this dependence of Nu on σ . Given that for $\sigma > 1$ viscosity is larger than thermal diffusivity, it is plausible that the vortical state is less prominent, and the current model is thus not relevant at higher σ .

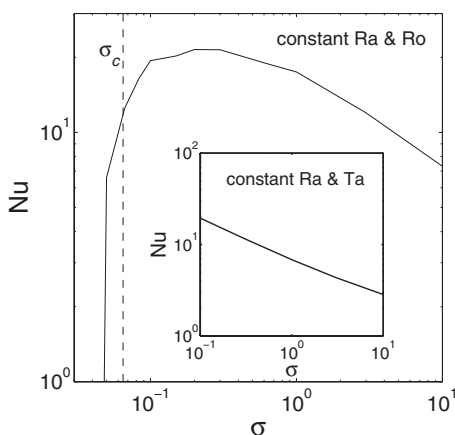


FIG. 11. Dependence of Nu on σ at constant $Ra=2.5 \times 10^6$ and constant $Ro=0.5$. The dashed line indicates the critical value σ_c from Chandrasekhar's theory (Ref. 4). Inset: Dependence of Nu on σ at constant $Ra=2.5 \times 10^6$ and constant $Ta=1 \times 10^8$.

VI. CONCLUDING REMARKS

Starting from the Navier–Stokes equations and some symmetry considerations, it was possible to derive a model for the vortical columnar plumes of rotation-dominated convection. The radial and vertical structures of the vortex as predicted by the model matched the features found in the DNS rather well. A calculation of the heat flux provided an upper bound that was found to be appropriate for the regime under study.

Still, the model has some shortcomings. There is an unknown constant in the model, for which only an upper bound is known. The termination of the radial extent of the vortex is unphysical. Also, the heat flux is dependent on the vertical coordinate and cannot match with the often-used definition of the averaged wall-normal temperature gradient (see, e.g., Ref. 14). This follows directly from the symmetry constraint on the temperature deviation from the conductive profile.

A comparison of the model results with DNS showed that the average vortex size was captured well. The dependence of the heat transfer on Ta was very satisfactorily represented in the model. When Ra is increased the upper bound for heat transfer in the model has a larger margin over the DNS results, but for the parameter range considered, it still gives a reasonable result. The relation with σ could not be checked directly to DNS results. A comparison to experiments and simulations in different geometries revealed that the Prandtl number dependence in the model is not well recovered. The range of validity of the model solution appears to be restricted to lower Prandtl numbers.

This study shows that the linearized Navier–Stokes equations not only provide information about the onset of instabilities but also possess interesting and relevant classes of solutions that fulfill certain symmetry requirements.

ACKNOWLEDGMENTS

We thank the anonymous referees for their very valuable remarks that led to a considerable improvement of this article. R.P.J.K. wishes to thank the Foundation for Fundamental Research on Matter (Stichting voor Fundamenteel Onderzoek der Materie, FOM) for financial support.

¹J. Proudman, "On the motion of solids in a liquid possessing vorticity," *Proc. R. Soc. London, Ser. A* **92**, 408 (1916).

²G. I. Taylor, "Experiments of the motion of solid bodies in rotating fluids," *Proc. R. Soc. London, Ser. A* **104**, 213 (1923).

³A. E. Gill, *Atmosphere-Ocean Dynamics* (Academic, New York, 1982).

⁴S. Chandrasekhar, *Hydrodynamic and Hydromagnetic Stability* (Oxford University Press, Oxford, 1961).

⁵A. P. Bassom and K. Zhang, "Strongly nonlinear convection cells in a rapidly rotating fluid layer," *Geophys. Astrophys. Fluid Dyn.* **76**, 223 (1994).

⁶J. H. P. Dawes, "Rapidly rotating thermal convection at low Prandtl number," *J. Fluid Mech.* **428**, 61 (2001).

⁷B. M. Boubnov and G. S. Golitsyn, "Experimental study of convective structures in rotating fluids," *J. Fluid Mech.* **167**, 503 (1986).

⁸B. M. Boubnov and G. S. Golitsyn, "Temperature and velocity field regimes of convective motions in a rotating plane fluid layer," *J. Fluid Mech.* **219**, 215 (1990).

⁹F. Zhong, R. E. Ecke, and V. Steinberg, "Rotating Rayleigh-Bénard convection: asymmetric modes and vortex states," *J. Fluid Mech.* **249**, 135 (1993).

- ¹⁰S. Sakai, "The horizontal scale of rotating convection in the geostrophic regime," *J. Fluid Mech.* **333**, 85 (1997).
- ¹¹P. Vorobieff and R. E. Ecke, "Turbulent rotating convection: an experimental study," *J. Fluid Mech.* **458**, 191 (2002).
- ¹²K. Julien, S. Legg, J. McWilliams, and J. Werne, "Rapidly rotating turbulent Rayleigh-Bénard convection," *J. Fluid Mech.* **322**, 243 (1996).
- ¹³M. Sprague, K. Julien, E. Knobloch, and J. Werne, "Numerical simulation of an asymptotically reduced system for rotationally constrained convection," *J. Fluid Mech.* **551**, 141 (2006).
- ¹⁴R. P. J. Kunnen, H. J. H. Clercx, and B. J. Geurts, "Heat flux intensification by vortical flow localization in rotating convection," *Phys. Rev. E* **74**, 056306 (2006).
- ¹⁵J.-C. Gascard, A. J. Watson, M.-J. Messias, K. A. Olsson, T. Johannessen, and K. Simonsen, "Long-lived vortices as a mode of deep ventilation in the Greenland Sea," *Nature (London)* **416**, 525 (2002).
- ¹⁶P. Wadhams, J. Holfort, E. Hansen, and J. P. Wilkinson, "A deep convective chimney in the winter Greenland Sea," *Geophys. Res. Lett.* **29**, 1434, DOI: 10.1029/2001GL014306 (2002).
- ¹⁷G. Budéus, B. Cisewski, S. Ronski, D. Dietrich, and M. Weitere, "Structure and effects of a long lived vortex in the Greenland Sea," *Geophys. Res. Lett.* **31**, L05304, DOI: 10.1029/2003GL017983 (2004).
- ¹⁸F. H. Busse, "Convection driven zonal flows and vortices in the major planets," *Chaos* **4**, 123 (1994).
- ¹⁹H. F. Goldstein, E. Knobloch, I. Mercader, and M. Net, "Convection in a rotating cylinder. Part 1. Linear theory for moderate Prandtl numbers," *J. Fluid Mech.* **248**, 583 (1993).
- ²⁰H. F. Goldstein, E. Knobloch, I. Mercader, and M. Net, "Convection in a rotating cylinder. Part 2. Linear theory for low Prandtl numbers," *J. Fluid Mech.* **262**, 293 (1994).
- ²¹H. T. Rossby, "A study of Bénard convection with and without rotation," *J. Fluid Mech.* **36**, 309 (1969).
- ²²C. Hunter and N. Riahi, "Nonlinear convection in a rotating fluid," *J. Fluid Mech.* **72**, 433 (1975).
- ²³Y. Liu and R. E. Ecke, "Heat transport scaling in turbulent Rayleigh-Bénard convection: effects of rotation and Prandtl number," *Phys. Rev. Lett.* **79**, 2257 (1997).
- ²⁴R. Verzicco and R. Camussi, "Prandtl number effects in convective turbulence," *J. Fluid Mech.* **383**, 55 (1999).
- ²⁵R. M. Kerr and J. R. Herring, "Prandtl number dependence of Nusselt number in direct numerical simulations," *J. Fluid Mech.* **419**, 325 (2000).